



Effect of Stress States on Twinning Behavior in Twinning-Induced Plasticity Steel

Joong-Ki Hwang

(Submitted January 12, 2019; in revised form April 25, 2019; published online August 7, 2019)

The effects of stress state on the twin structures and kinetics in twinning-induced plasticity (TWIP) steel have been investigated to understand the twinning behaviors in more detail. Twinning behaviors of tension, compression, wire drawing, and caliber rolling were evaluated and compared using the EBSD technique, TEM measurement, and Schmid factor analysis. Twin structures, such as twin thickness, twin variant, twin shape, and twin kinetics were different with stress states. The specimen under compressive stress had wavy-shaped twins, less twin variant, lower twin thickness, and more twin volume fraction in comparison with the specimen under tensile stress. The different structures and kinetics of deformation twin with stress state were highly related to the grain rotation during plastic deformation. Under tensile stress, the grain rotation to $\langle 111 \rangle$ orientation, twinning-favored regions by Schmid factor analysis, encouraged the lateral growth of twins, more twin variants, and straight-type twins, while the grain rotation to $\langle 110 \rangle$ orientation under compressive stress suppressed the twin growth and twin variant and developed wavy-shaped twins. Drawn wire and caliber-rolled wire had both twin features under tensile and compressive stress states and higher twin volume fraction since complex stress state that combined tension and compression was applied in these processes. The hardness values were strongly related to the twin volume fraction with strain and stress state.

Keywords deformation twin, grain rotation, stress state, twinning-induced plasticity (TWIP) steel

1. Introduction

Improving the fuel efficiency of vehicle and the safety of passenger is a big trend in iron and steel making industry for automotive applications. The steels thus need to possess high strength to decrease the overall car weight and good formability to form complex parts by plastic forming process. However, simultaneously improving the strength and formability of metals remains a challenge. Consequently, this contradictory requirement has led to search for new high-performance materials. High strain hardening rate has been observed in some face-centered cubic (FCC) alloys with low stacking fault energy (SFE) such as austenitic stainless steels, transformation-induced plasticity (TRIP) steels, and twinning-induced plasticity (TWIP) steels. Among them, TWIP steels have received considerable attentions over the past few decades due to the excellent combination of strength and ductility combined with outstanding energy absorption capacity stemming from their high strain hardening rate (Ref 1-6).

The high strain hardening rate of TWIP steel can be classically explained by dynamic strain aging (DSA) and so-called dynamic Hall–Petch effect. DSA is attributed to the pinning of mobile dislocations by the small solute atoms diffusing within the matrix (Ref 6-9). Especially in TWIP

steels, Dastur and Leslie (Ref 6) suggested that DSA is originated from the strong interactions between solute atom dipoles (C-Mn) and dislocation strain field. It is generally accepted that deformation twins increase strain hardening rate by the twin boundaries that subdivide the parent austenite grains and act as effective barriers to subsequent dislocation glide, often called dynamic Hall–Petch effect or TWIP effect (Ref 10-12). The relationship between strain hardening rate and deformation twinning has been extensively investigated as a function of the strain through tensile tests (Ref 13-17). Barbier et al. (Ref 13) found that twinning behavior is strongly related to the strain hardening rate in Fe-22Mn-0.6C TWIP steel. According to the twinning behaviors, they divide the plastic deformation region into five stages with strain. Renard and Jacques (Ref 14) reported that twin volume fraction is highly related to the strain hardening rate in Fe-20Mn-1.2C TWIP steel.

It is well known that the mechanism of twin formation is strongly affected by SFE (Ref 18-21). Although SFE mainly controls the twinning behavior in TWIP steels, the twinning kinetics depends on the other several factors such as grain size/orientation, strain rate, and stress state (Ref 1, 4). In numerous studies, it has been shown that the twinning behavior strongly depends on the grain orientation. The effect of grain orientation on twinning behaviors is logically explained from the Schmid factor analysis (Ref 4, 22-27) through the uniaxial tension and compression tests. Gutierrez-Urrutia et al. (Ref 4) observed that the twinning behavior fully complies with Schmid's law at low strain, while twins occur in unfavorably oriented grains at high strain in Fe-22Mn-0.6C TWIP steel during tensile test. It is reported that strong $\langle 111 \rangle$ and weak $\langle 100 \rangle$ textures are developed and grains close to $\langle 111 \rangle$ have twins due to the lower twinning stress than slip during tensile test (Ref 24). Yang et al. (Ref 25) reported that the grain rotation influences the twinning behavior using EBSD techniques and the Schmid

Joong-Ki Hwang, School of Mechanical Engineering, Tongmyong University, Busan 48520, Republic of Korea. Contact e-mail: jkhwang@tu.ac.kr.

factor analysis in Fe-33Mn-3Al-3Si TWIP steel during tensile test. They reported that grain rotations activate the twin deformation mechanism because twins tend to occur close to $\langle 111 \rangle$ grain. In case of compression, strong $\langle 110 \rangle$ texture is developed in FCC materials. Meng et al. (Ref 26) reported that grain rotations suppress the twin deformation mechanism using Fe-33Mn-3Al-3Si TWIP steel because twins tend to occur close to $\langle 100 \rangle$ grain under compressive stress.

The twinning behavior in TWIP steels is susceptible to the imposed stress state because twinning mechanism strongly depends on the grain orientation. Renard et al. (Ref 28) reported the influence of stress state on the twin kinetics and strain hardening behavior using Fe-20Mn-1.2C TWIP steel. They compared three different stress states such as uniaxial tension, simple shear, and rolling. They reported that twin volume fraction, morphology, and twin variants are dependent on the stress state and the strain hardening rate is larger for uniaxial tension, then rolling, and finally simple shear. They also reported that more twins with thinner, less parallel, and confined within individual grains lead to the higher strain hardening rate. This means stress states affect the twinning behaviors and finally mechanical properties. In addition, Idrissi et al. (Ref 29) reported that the twin shape as well as twin volume fraction is highly related to the strain hardening rate by the comparison of microstructure in Fe-Mn-C and Fe-Mn-Si-Al TWIP steels.

Although many studies have been conducted on the twinning behaviors using tensile, compressive, and cold rolling tests in TWIP steels, the relationship between imposed stress state and twin structures was hardly found despite the dependence of mechanical properties on twin structures (Ref 28, 29). Also, only a few studies have been reported on the other stress states except for tension, compression, and cold rolling (Ref 28). Consequently, the effect of stress state on twin structures and kinetics of TWIP steels is still poorly understood. The present study therefore deals with the effects of stress state on the twin structures and kinetics in TWIP steel to understand the twinning behaviors in more detail. The tensile, compressive, wire drawing, and caliber rolling tests were conducted, and twinning behaviors of each stress state were compared using the electron backscatter diffraction (EBSD) technique, transmission electron microscopy (TEM) measurement, and Schmid factor analysis.

2. Experimental

The analyzed chemical composition (in wt.%) of TWIP steel used in this study was Fe-19.94Mn-0.6C-1.03Al. A cast ingot of 125 mm in thickness was prepared by induction melting. The SFE calculated by the thermodynamics model of Saeed-Akbari et al. (Ref 19) was 23.5 mJ/m^2 , indicating that the primary plastic deformation mode is deformation twinning rather than martensitic transformation or dislocation glide at room temperature (Ref 18, 21, 30). To obtain uniform microstructure and remove Mn segregation, the ingot was homogenized at $1200 \text{ }^\circ\text{C}$ for 12 h. Then, it was directly hot-rolled down to the final thickness of 20 mm at finishing temperature of above $950 \text{ }^\circ\text{C}$, followed by air cooling. Round wires with a diameter of 15 mm for wire drawing test and 13 mm for caliber rolling test were machined from the hot-rolled plate along the hot-rolling direction.

The wires with the initial diameter of 15 mm were drawn at a pulling speed of 0.0083 m/s with the same direction in every drawing step using the single type draw bench machine at room temperature. To remove the oxide scale on the wire surface, chemical pickling with 12.5% HCl was carried out on the wire prior to drawing test. The lubricant with a chemical composition of MoS_2 was applied on wire surface to reduce the friction between wire and drawing dies. The die angle was 12° , and the average reduction of area (RA) per pass was about 10% (Ref 31).

For caliber rolling test, wires with the initial diameter of 13 mm were rolled at the average RA per pass of 10% with the grooves of oval and round shapes without lubricant at room temperature. Figure 1 shows the schematic of caliber rolling process and cross-sectional shape of workpiece. The shape of workpiece was oval at odd passes and round at even passes, i.e., over-round sequence. The workpiece was rotated by an angle of 90° at every pass for the next rolling step due to the horizontal-type caliber rolling machine in this study (Ref 32). The working roll had a diameter of 400 mm, and rolling speed was set as 5 RPM to ignore the effect of temperature rise. During wire drawing and caliber rolling tests, RA is calculated using following equation:

$$\text{RA} = \frac{A_0 - A_f}{A_0} \times 100 (\%) \quad (\text{Eq 1})$$

where A_o and A_f are the initial and final cross-sectional areas of wire, respectively. The effective strain of wire, ϵ , is calculated by area change during process using following equation:

$$\epsilon = \ln \frac{A_0}{A} = 2 \ln \frac{d_0}{d} \quad (\text{Eq 2})$$

where d_0 denotes initial diameter of wire. Round-shape tensile specimens having a gauge length of 25 mm and gauge diameter of 5 mm were machined along the hot-rolling direction. Room temperature tensile tests were carried out at an initial strain rate of 10^{-3} s^{-1} using an Instron machine equipped with a contact-type extensometer. To examine the microstructure development in detail, interrupted tensile tests were performed at the various levels of strain as shown in Table 1.

Compression specimens with the dimension of 10 mm in diameter and 15 mm in height were machined from the hot-rolled plate along the rolling direction and then compressed at a strain rate of 10^{-3} s^{-1} using an Instron machine at room temperature. Interrupted tests were also performed to the different levels of strain to examine the microstructure as summarized in Table 1. The effective strain of compressive-strained specimen is calculated by the following equation:

$$\epsilon = \ln \frac{h_0}{h} \quad (\text{Eq 3})$$

where h_o and h mean the initial and final height of compression specimen, respectively. The Vickers hardness was measured with stress state using 1 kg weight over the cross section perpendicular to the loading axis.

The microstructure was characterized by EBSD and TEM. To prepare the specimens for EBSD observation, mechanical and chemical polishing was applied using diamond pastes down to $1 \mu\text{m}$ and then colloidal silica slurry for about 1.2 ks. FEG SEM with a TSL EBSD system was used at 20 keV to acquire EBSD data. The specimen was tilted at approximately 70° relative to normal incidence of electron beam, and the step

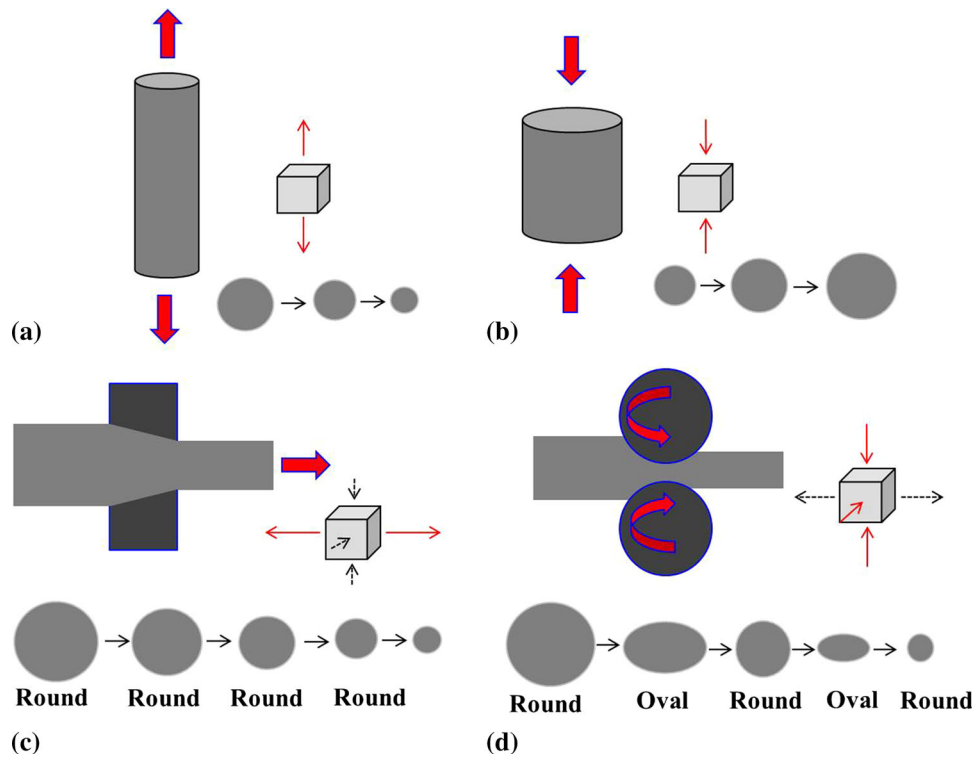


Fig. 1 Schematic of stress state and cross-sectional shape of specimen during (a) tension, (b) compression, (c) wire drawing, and (d) caliber rolling

Table 1 Effective strain of characterized specimens with stress state in this experiment

Stress state	Effective strain of characterized specimens					Comments
Tension	0.049	0.095	0.18	0.34	...	Interrupted test
Compression	0.034	0.08	0.17	0.30	0.43	Interrupted test
Wire drawing	0.13	0.26	0.39	0.50	...	10% RA per pass
Caliber rolling	0.13	0.25	0.35	0.45	...	10% RA per pass

size of $0.1 \mu\text{m}$ was used for obtaining EBSD data. The OIM software was applied for the post-processing of EBSD data. The jet-polished 3-mm disk thin foil was prepared to observe TEM images, and TEM was operated under at 200 kV. Microstructural characterizations were performed on the cross-sectional area of samples perpendicular to the loading axis.

3. Results and Discussion

3.1 Evolution of Microstructure and Texture

As shown in Fig. 2, the initial hot-rolled steel consists of recrystallized equiaxed grains with an average grain size of $28 \mu\text{m}$. Many annealing twins were seen, but no deformation twin was observed. Numerous studies have focused on the texture evolution during plastic deformation since texture affects microstructure and mechanical properties of material. EBSD techniques are the effective tool to characterize both microstructure and texture; therefore, the microstructure and

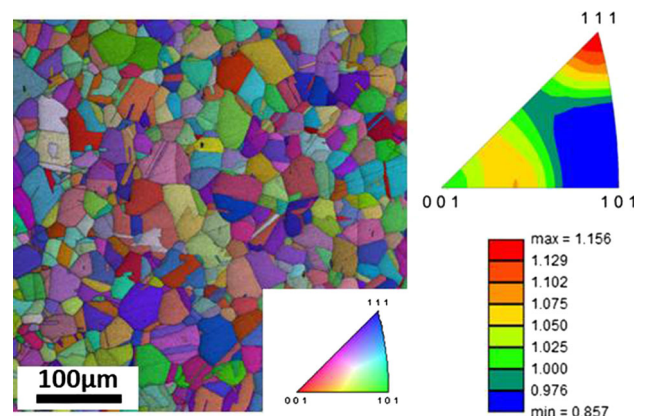


Fig. 2 EBSD inverse pole figure (IPF) map of hot-rolled steel along the rolling direction (RD)

texture including twinning behavior with stress state were analyzed using EBSD. Figure 3 and 4 shows the EBSD inverse pole figure (IPF) maps and the corresponding textures of tensile

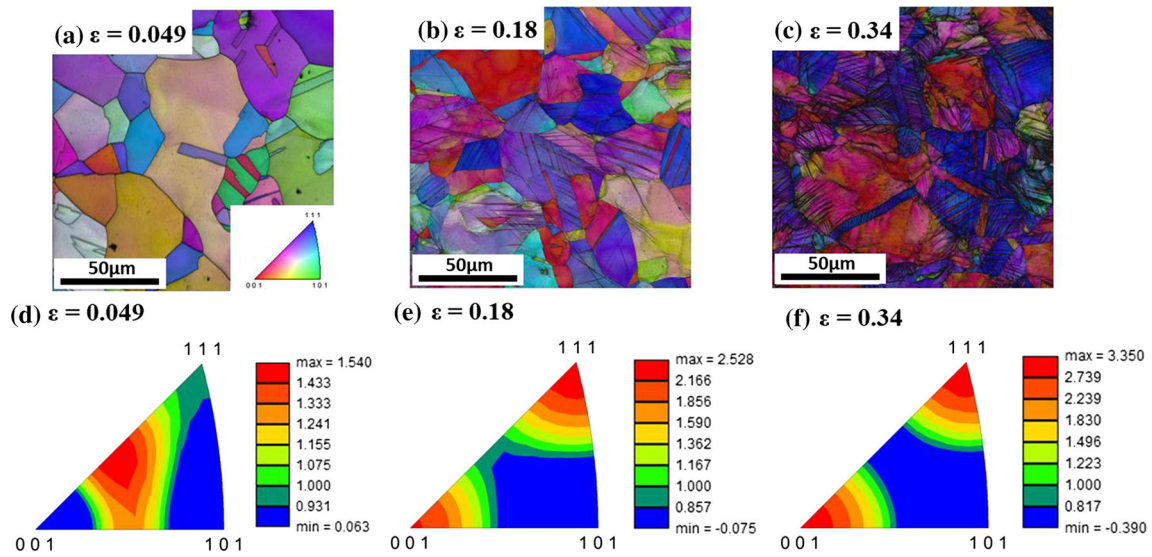


Fig. 3 EBSD (a-c) IPF maps and (d-f) corresponding textures of tensile-strained specimen at the true strain of 0.049, 0.18, and 0.34

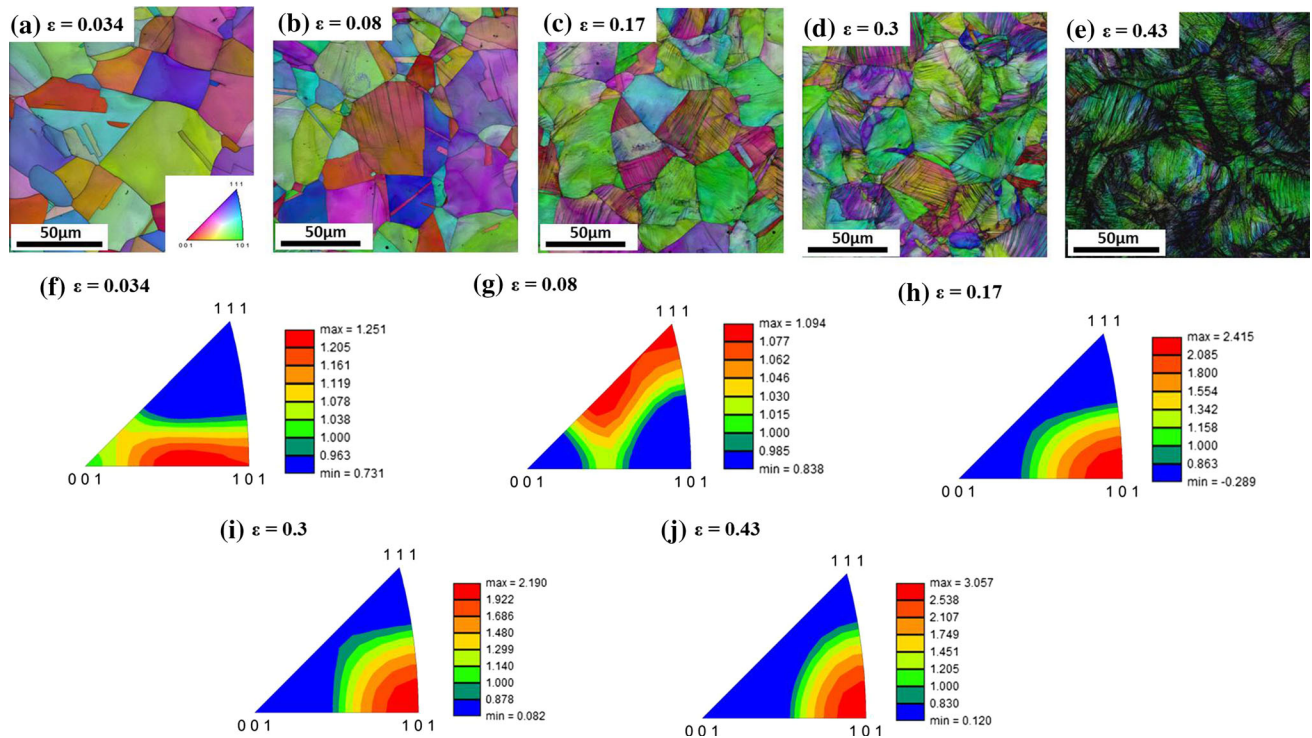


Fig. 4 EBSD (a-e) IPF maps and (f-j) the corresponding textures of compressive-strained specimen at the strain of 0.034, 0.08, 0.17, 0.3, and 0.43

and compressive-strained specimens deformed at various true strains. EBSD observations were carried out on the cross section of samples perpendicular to the straining direction. Parallel thin lines within grain are the deformation twin bundles, which consist of several individual twins (Ref 33). The point counting method in OIM software was applied to distinguish $\Sigma 3$ twin boundaries in the austenitic matrix. It should be noted that the individual thin twins cannot be discerned by EBSD measurement originated from its limited resolution.

No deformation twin was detected under tensile stress at the strain of 0.049; on the other hand, twin bundle was seen near $\langle 100 \rangle$ grains under compressive stress at the strain of 0.034. The twin volume fraction was increased with strain in both stress states. Meanwhile, the orientation dependence of twin activity was observed: Twins started to appear close to the grains of $\langle 101 \rangle$ and $\langle 111 \rangle$ orientations (Fig. 3b) under tensile stress, followed by increased in the similar grains (Fig. 3c), whereas twins tend to occur in the grain of $\langle 100 \rangle$ orientation under compressive stress (Fig. 4a-c). Interestingly, the shape of deformation twin was different with stress state.

Most of the twins were the shape of straight line in the tensile specimens, whereas wavy-shaped twins were developed as the strain was increased in the compressive specimens, which is consistent with the previous result by Meng et al. (Ref 26). Moreover, more twin variants tend to develop under tensile stress with strain. In other words, two twin variants were observed under tensile stress, whereas many grains had single twin variant under compressive stress. For convenience, T1 is defined as primarily occurred twins with single twin variant, and T2 is defined as secondarily occurred twins by other twinning systems in each grain, hereafter. Typically, T1 and T2 were observed with specific angle, i.e., 70.5° , stemming from their conjugate twinning systems in FCC structure. It should be noted that T1 and T2 are the first-order twins.

In case of grain orientation, $\langle 111 \rangle$ and $\langle 100 \rangle$ textures were developed under tensile stress and $\langle 110 \rangle$ texture was developed under compressive stress, which is well known in FCC alloys (Ref 13, 34). Nevertheless, it is worth noting that the textures were not developed in the tensile-strained sample

under the strain of 0.049 (Fig. 3d) and the compressed samples under the strain of 0.034 (Fig. 4f) 0.08 (Fig. 4g) due to the lower strain to develop final type texture. These EBSD results explain that the imposed stress state has a significant effect on texture and microstructure in TWIP steel.

The microstructure and texture were also evaluated during wire drawing using EBSD at the strain of 0.13, 0.26, and 0.5 as shown in Fig. 5. The cross section of samples perpendicular to the drawing direction was observed. These maps brought about a contrast between center area and surface area. A few grains seem to have deformation twins at the strain of 0.13 at center area; in contrast, many grains of surface area contained deformation twins with single or two twin variants at the same strain. That is, surface area had more twin volume fraction and more twin variants compared to center area. Three twin variants, for instance, were operated in some grains at surface area despite the low strain of 0.13. Furthermore, the twins of surface area had a more wavy shape in comparison with center area. All the grains of surface area had twins at the strain of

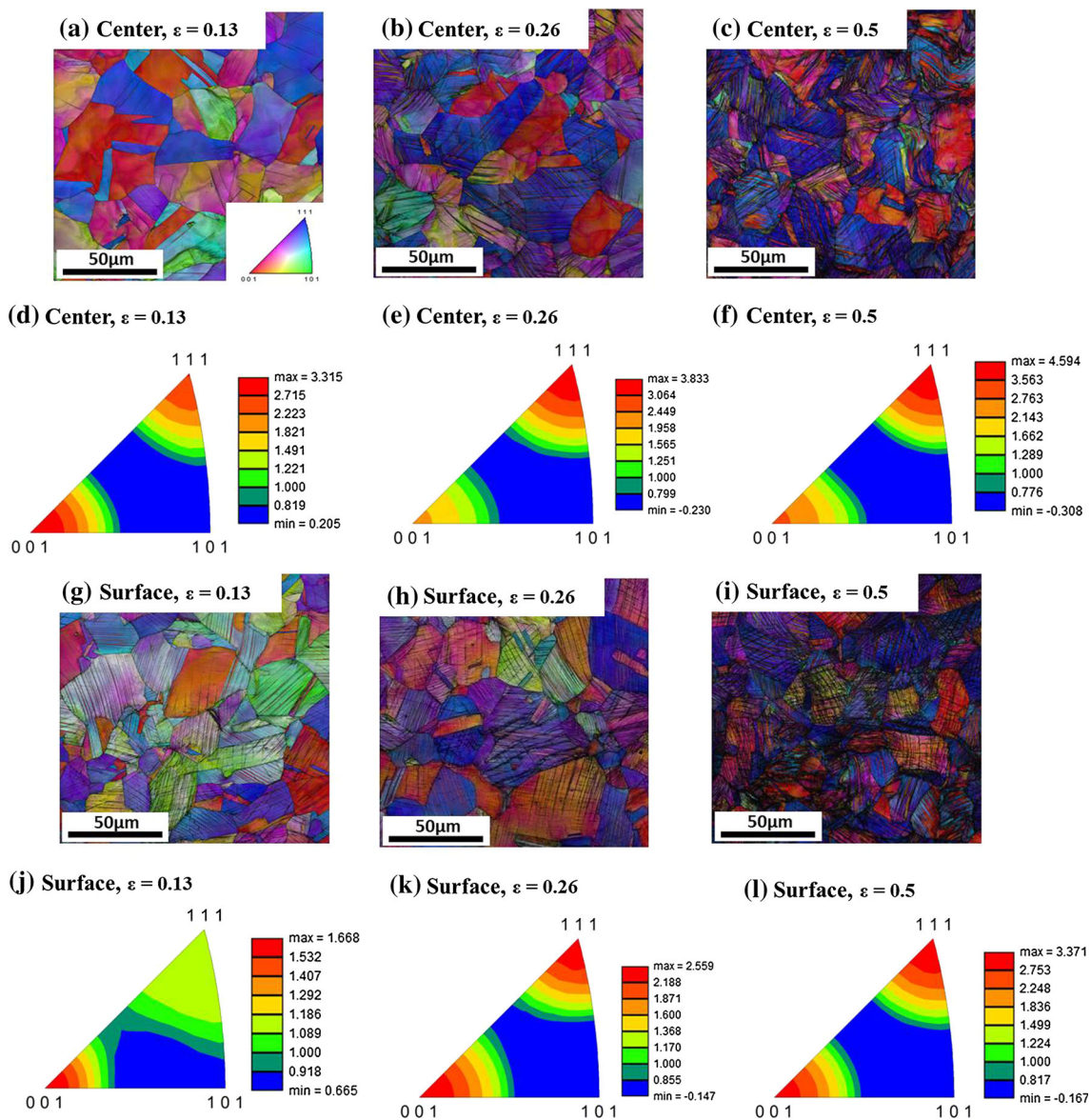


Fig. 5 EBSD IPF maps and the corresponding textures of drawn wire at the drawing strain of 0.13, 0.26, and 0.5 with area

0.25. These different twinning behaviors with area were explained by the relatively higher strain and more complex stress states combining compression, tension, and shear at surface area in comparison with center area (Ref 35, 36). In other words, the relative high strain and complex stress state accelerate the twinning activities (Ref 27, 37). Interestingly, many deformation twins were observed in grains oriented close to the $\langle 111 \rangle$, whereas twin was seldom observed in grains close to the $\langle 100 \rangle$ at center area despite heavy plastic deformation of 0.5 (Fig. 5c). The twinning behavior such as twin shape, volume fraction, and twin variants of center area was similar to the results of tensile test (Fig. 3). The volume fraction of grains close to $\langle 111 \rangle$ orientation increased, but that of $\langle 100 \rangle$ orientation decreased, and $\langle 110 \rangle$ texture almost disappeared with increasing strain. Numerous studies have reported that strong $\langle 111 \rangle$ and weak $\langle 100 \rangle$ are the stable deformation textures in drawn FCC metals regardless of SFE (Ref 34, 38). However, due to the uneven strain distribution and the difference in stress state along the radial direction, the distribution of the $\langle 111 \rangle$ and $\langle 100 \rangle$ fiber textures is inhomogeneous with area (Ref 27).

The EBSD maps were measured at cross-sectional planes perpendicular to caliber rolling direction as shown in Fig. 6. Many grains had deformation twins, and some grains contained deformation twins with two or three twin variants despite the low strain level of 0.13. The center area had a larger number of deformation twins than the surface area due to the higher strain (Ref 32). Moreover, the twins at center area had more wavy shape in comparison with those at surface area. At the strain of 0.25, all the twins did not appear in the IPF map because twins could not be discerned at high strains due to the poor image quality, especially at center area.

In order to analyze the texture at each area in more detail, texture analysis was also conducted. From the initially weak texture (Fig. 2), the volume fraction of $\langle 111 \rangle$ grains increased, which is similar to that of drawn wire, but not strong compared to drawn wire. The developed texture of caliber-rolled wire depended on the areas of cross section (Ref 32). The surface area had strong $\langle 111 \rangle$ texture compared to the center area.

To have a quantitative comparison on the twinning behaviors, the relative twin volume fraction was measured with stress

state using the calculation of total twin length by EBSD techniques as shown in Fig. 7(a). Most of the twin boundaries in FCC materials are the $\Sigma 3 = 60^\circ \langle 111 \rangle$ and $\Sigma 9 = 38.9^\circ \langle 101 \rangle$ (Ref 39). In particular, twin boundaries with $\Sigma 3$ misorientation type are dominant; hence, the coherent $\Sigma 3$ twin boundaries having a misorientation angle of 60° between twin and matrix around $\langle 111 \rangle$ axis were quantified and compared. The tolerance angle from exact twin relationship was set as 6° according to the Palumbo–Aust criterion (Ref 40). Then, the total length of this value was divided by the total measured area, $\mu\text{m}/\mu\text{m}^2$. Obviously, the twin volume fraction, i.e., total twin length, progressively increased with strain. The difference of twin volume fraction with stress state was clearly observed. A significant increase in twin volume fraction was observed during caliber rolling and wire drawing, especially the center area of caliber-rolled wire and the surface area of drawn wire. The twin volume fractions during tensile and compressive tests were low at all the strain levels compared to the other complex stress states. Compared to the tensile-strained specimen, compressive-strained specimen had higher twin volume fraction at the same strain. These results mean that the twin volume fraction of TWIP steel was strongly dependent on the applied stress state during plastic deformation. To analyze the behavior of twin variants with stress state, grains with twins and T2 were evaluated as shown in Fig. 7(b). The specimens under uniaxial stress such as tension, compression, and center area of drawn wire tend to have single twin variant, whereas the complex stress states such as caliber rolling and surface area of drawn wire were easy to make two or three twin variants. Interestingly, compared to the tensile specimen, compressive specimen had lower T2 although it had higher twin volume fraction. Figure 7(c) shows the average hardness as a function of effective strain with stress state. The hardness values with strain state were strongly related to the twin volume fraction: both twin volume fraction and average hardness were larger for caliber rolling, wire drawing, then compression, and finally tension.

3.2 Evolution of Twin Structures

Twin volume fraction and structures are highly related to strain hardening rate in TWIP steels (Ref 14, 28, 29). It is not

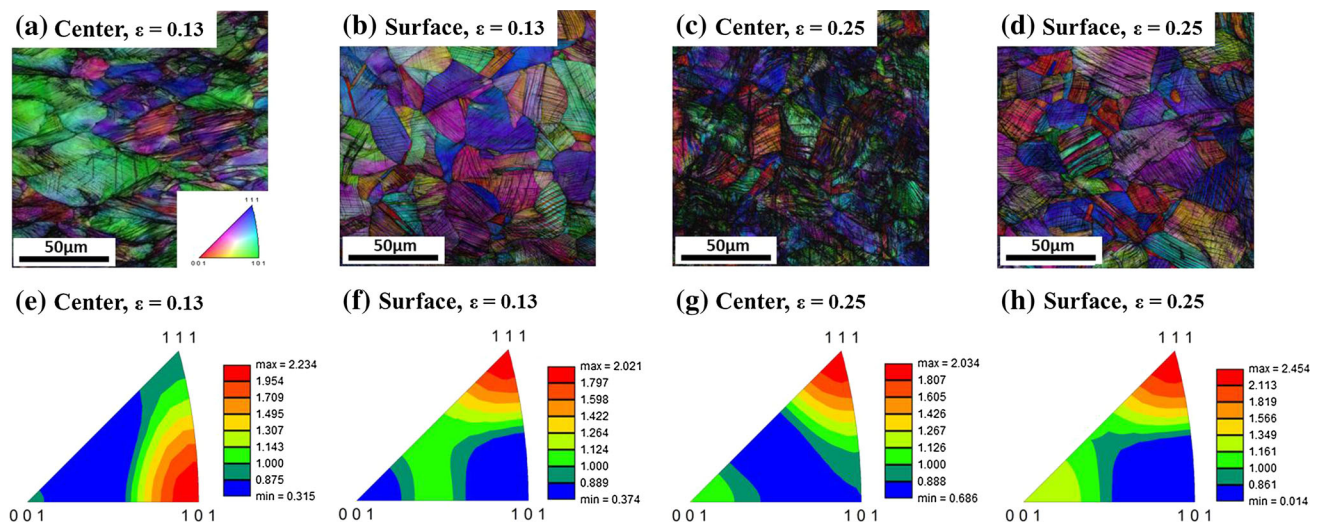


Fig. 6 EBSD (a-d) IPF maps and (e-h) the corresponding textures of caliber-rolled wire at the effective strain of 0.13 and 0.25 with area

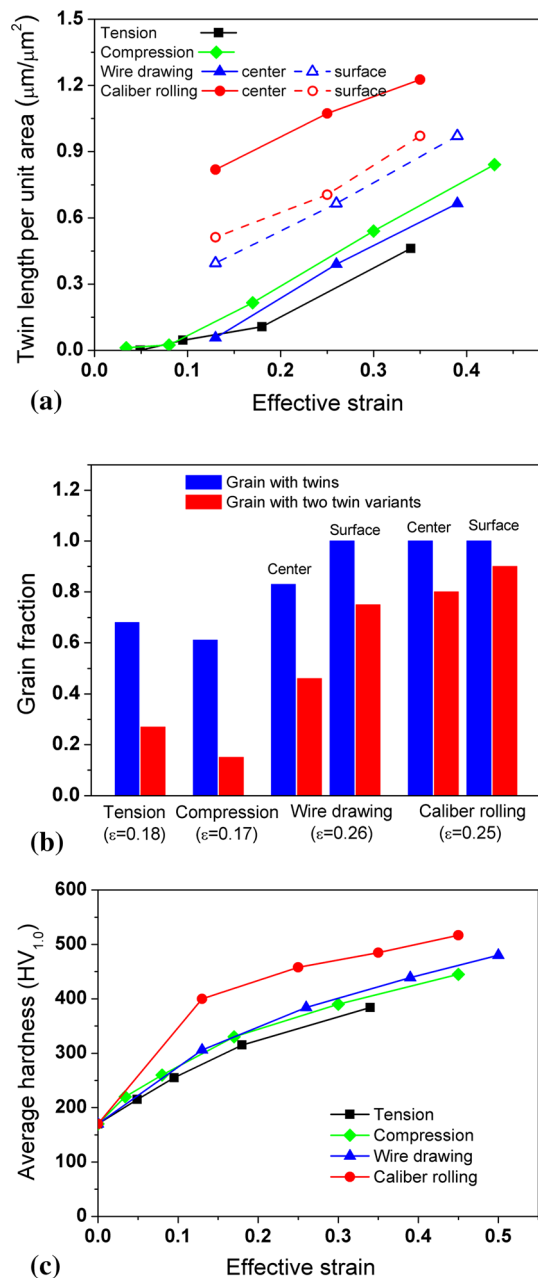


Fig. 7 Comparison of (a) variation in length per unit area of deformation twins as a function of strain, (b) grain fraction with deformation twins, and (c) average hardness values as a function of strain with stress state

easy to analyze twin structures using SEM or EBSD due to their limited resolution; therefore, the twinning structures with stress states were identified using TEM. Figure 8 shows TEM images along the $\langle 110 \rangle$ zone axis of tensile- and compressive-strained specimens at the true strain of 0.18 and 0.17, respectively. As the zone axis of TEM measurement was close to $\langle 110 \rangle$ axis, the twins in the plane of $(-11-1)$ and (-111) can be edge on, whereas the twins in (111) and $(11-1)$ planes are inclined. We can thus measure the thickness of twin in the edge on planes. The straight and thin lines were identified twins, revealing that twins observed by EBSD were twin bundles, which are composed of several individual twins in the thickness of 5-60 nm. More interestingly, the twin thickness of compressive-

strained specimen was a little bit thinner than that of tensile-strained specimen. At each stress state, 20 TEM micrographs with more than 140 individual twins were used for statistical analysis on twin thickness as shown in Fig. 8(g). The average twin thickness was about 27 nm in tensile-strained specimen and about 22 nm in compressive-strained specimen. It is well known that deformation twins generally nucleate from grain boundaries, grow into the grain inside, and finally shear the whole grains. Clearly, it was observed that deformation twin was stopped at high angle grain boundaries regardless of stress state (Fig. 8c and f). As shown in Fig. 8(f), relatively thick twin was determined to be an annealing twin because it did not shear the whole grain.

Figure 9 shows representative microstructures of center and surface area of drawn wire at the strain of 0.26 and 0.5. T1 tends to occur at center area; on the other hand, both T1 and T2 were well observed at surface area. It is clearly seen that surface area had more twin volume fraction than center area. The twin thickness of surface area was thinner than that of center area due to the compressive stress state at surface area. Some T2 intersected T1 as a whole, but some T2 stopped lengthening at the boundary of T1 (white circle in Fig. 9b). This different configuration of T1 and T2 has an influence on the mechanical properties in TWIP steel (Ref 41, 42). It is worth noting that the generation of multi-twinning system can reduce the mean free path of dislocations more effectively (Ref 43). Twins with wavy shape were observed at high strain because early formed twins can be bent or distorted along the drawing direction, which is also observed in EBSD, especially under compressive stress (Fig. 4). The twin volume fraction and twin variants observed by TEM were in good agreement with those observed by EBSD (Fig. 5).

Figure 10 shows the TEM images of caliber-rolled wire at the strain of 0.25 with area. As shown in Fig. 10(a), the dislocation density was higher at twin interfaces, which supported that twin boundaries acted as obstacles to dislocation movements. Figure 10(b) shows the twin bundle composed of several nano-scale twins of 10-60 nm in thickness, and twin thickness and twin spacing (distance between neighboring twins) in twin bundles were almost same. T1 tends to occur at center area, whereas both T1 and T2 were well observed at surface area. The intersection of T1 and T2 was easily recognizable as shown in Fig. 10(c) and (d): The two twin variants sheared each other. The intersection between T1 and T2 made complex configuration.

From the above EBSD and TEM observations with stress state, Fig. 11 summarizes the structures of deformation twin during plastic deformation in TWIP steel. Most of twins in primary and conjugate twinning systems, i.e., T1 and T2, cut through each other as shown in TEM images. Mahajan and Chin (Ref 44) reported that the Shockley partials dislocations gliding on the $(-11-1)$ plane undergo dissociation at the (-111) coherent boundary to accomplish the T1 and T2 intersections. Meanwhile, relatively thin T2 intersected the existing T1 with the manner of straight line, resulting in forming a ladder-like configuration between two twins, whereas some T2 sheared the T1 with the manner of stair-like way. Mullner et al. (Ref 45) reported that the stair-like interaction of two twins made second-order twin that is formed within the already existing twinned regions. They also showed that second-order twin is energetically favorable. A close observation shows that some twins were blocked by twin boundaries, i.e., T2 was hindered from lengthening at the interface of T1, although they were

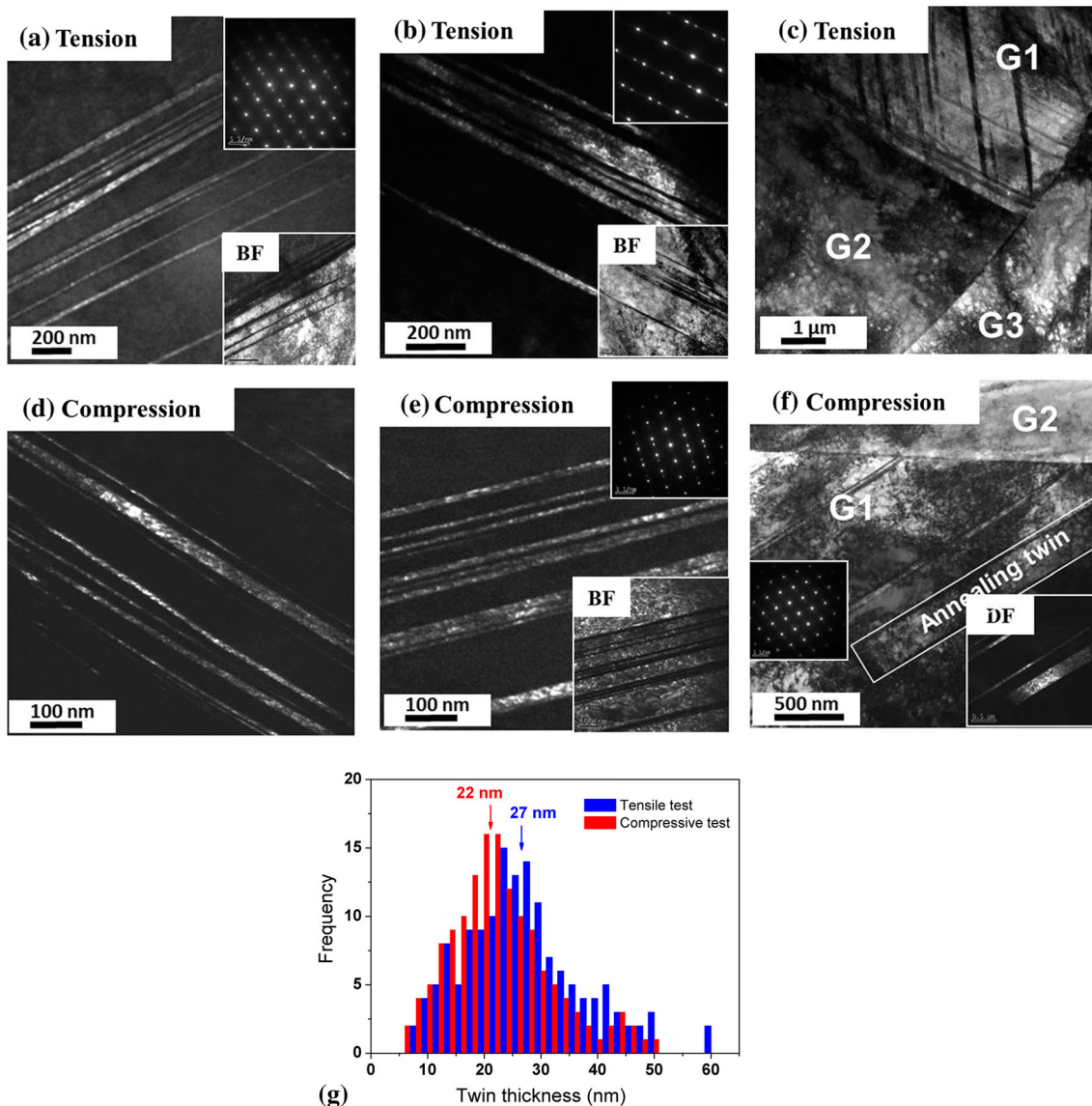


Fig. 8 Comparison of TEM images along the $\langle 110 \rangle$ zone axis under (a-c) tensile stress at the true strain of 0.18, (d-f) compressive stress at the true strain of 0.17, and (g) twin thickness of tensile and compressive-strained specimens

hardly observed. According to the Bonisch et al. (Ref 46), T2 approaching T1 was arrested at the barrier interface of T1, which means T2 was transfer into the primary twinning system, leaving behind residual dislocations. This residual dislocations may initiate the other twins since twin boundaries can act as effective sources for twinning dislocations (Ref 47), resulting in the intersection of T1 with further strain. The transmission and arrest of T2 at the interface of T1 may be dependent on the Schmid factors of each twinning systems. In contrast, it is also possible to explain that T2 was initiated at the interface of T1 as shown in Fig. 11. More details on the twin–twin interactions of FCC metals can be found elsewhere (Ref 44, 46, 48). Overall, the complex intersection configuration between T1 and T2 can reduce the mean free path of dislocations effectively, i.e., the refinement of austenite grains by twins, resulting in preventing the strain hardening rate drop at a higher strain level (Ref 13, 46, 49).

3.3 Schmid Factor Analysis

It is well known that slip and twin are competitive and/or cooperative deformation mechanisms depending on the SFE, strain rate, grain size/orientation in TWIP steels (Ref 4, 18, 24, 50-53). Especially, the twin mechanism strongly depends on the grain orientation because deformation twins occur by a strain driven external force in nature, which means stress state strongly affects the twinning behaviors. Theoretically, in order to evaluate the grain orientation dependence of deformation twinning in polycrystalline metals, Taylor factor analysis is needed (Ref 54), while several researchers have well explained the twinning behaviors using Schmid factor analysis in polycrystalline TWIP steels (Ref 4, 25-27) although Schmid's law is less appropriate for polycrystalline metals. This means twin activity in TWIP steels can be predicted using both Taylor factor analysis and Schmid factor analysis. Schmid factor

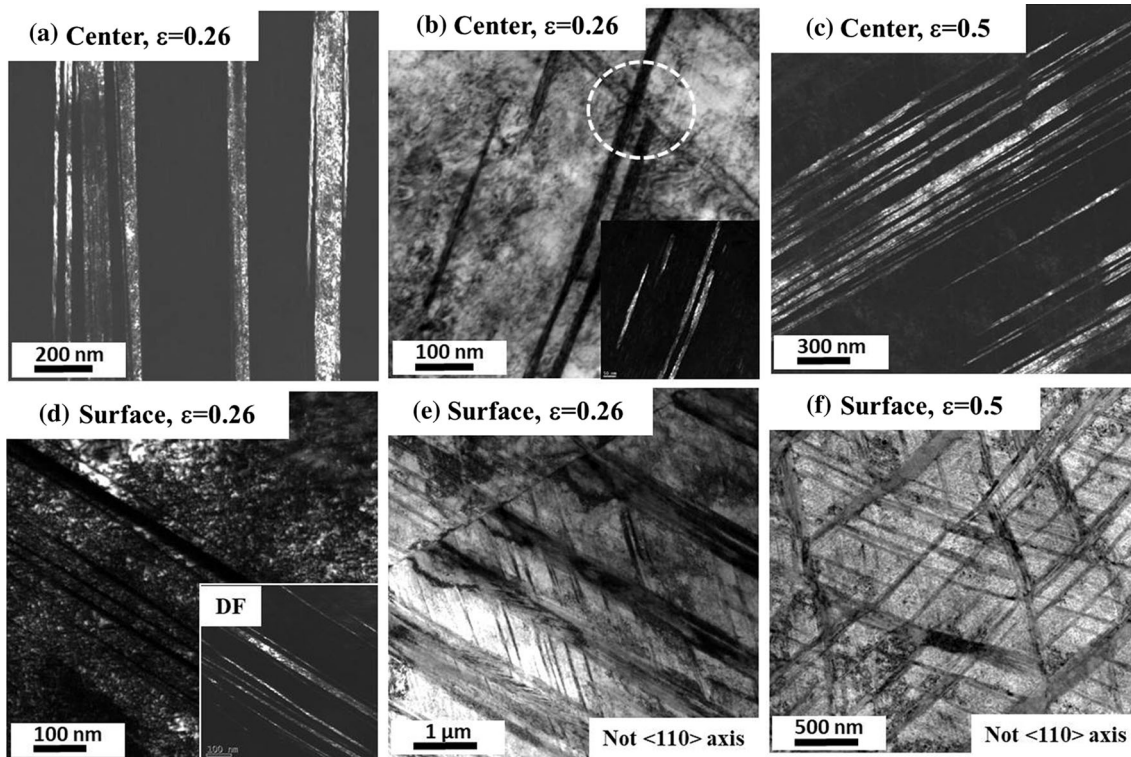


Fig. 9 TEM images of (a-c) center area and (d-f) surface area of drawn wire along the $\langle 110 \rangle$ zone axis

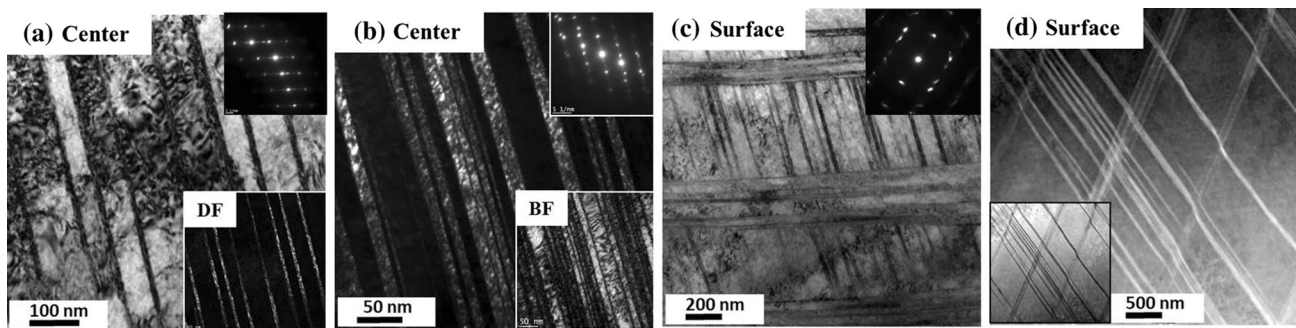


Fig. 10 TEM images of (a, b) center area and (c, d) surface area of caliber-rolled wire at the strain of 0.25 along the $\langle 110 \rangle$ zone axis

analysis is easier and simpler to understand and apply in metals than Taylor factor analysis. Schmid factor analysis was thus applied to analyze the grain orientation dependence of deformation twinning. The Schmid factor for leading partial dislocation was considered as Schmid factor for twinning. Since the Schmid factor for the leading partial dislocation is different under tensile stress and compressive stress (Ref 10), the twinning behavior in FCC crystals is asymmetric, which means the deformation behavior by twinning has a directionality with stress state (Ref 55). This is very different from the moving mechanism of perfect dislocation. Figure 12 depicts the maximum Schmid factor contours for slip, twin for tension, and twin for compression (Ref 22, 27). Schmid factors were calculated for the twinning of (111)[11-2] systems at a loading axis in the orientation triangle. Due to the directionality of deformation twinning, the higher Schmid factors for twin occurred in between $\langle 110 \rangle$ and $\langle 111 \rangle$ under tensile stress and close to $\langle 100 \rangle$ under compressive stress.

Figure 13 shows the Schmid factor contour under tensile stress to predict a twinning ability with grain orientation. This contour was deduced by calculating the ratio of Schmid factors for tension twin to Schmid factors for slip. It shows the favorable and unfavorable grain orientations for twinning under the assumption of equal critical resolved shear stress (CRSS) for slip and twinning (Ref 4, 22, 25, 26). According to these contours, tension along $\langle 111 \rangle$ and $\langle 110 \rangle$ was a favorable orientation for twinning because the Schmid factors for tension twin have a higher value than the Schmid factors for slip; on the other hand, grains close to $\langle 001 \rangle$ orientation tend to deform by slip mechanism under tensile stress. The contour for Schmid factor analysis under compressive stress state was also drawn as shown in Fig. 14 based on the same procedure above. The similar analysis has already been done by Yang and Meng et al. (Ref 25, 26), and Gutierrez-Urrutia et al. (Ref 4) in TWIP steels.

The closed circles depicted in orientation triangle mean twinned grains, and open circles mean non-twinned grains based

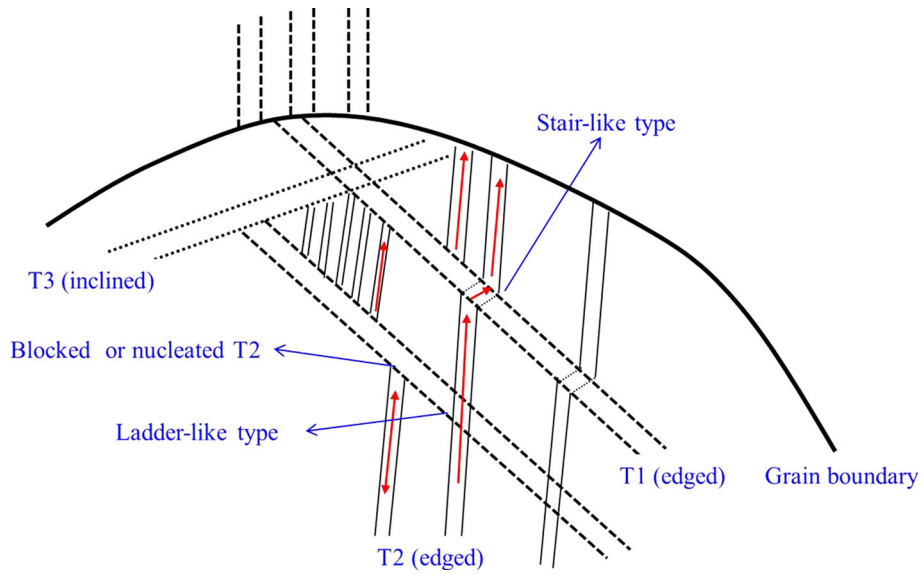


Fig. 11 Schematic showing the typical structure of deformation twin in TWIP steel

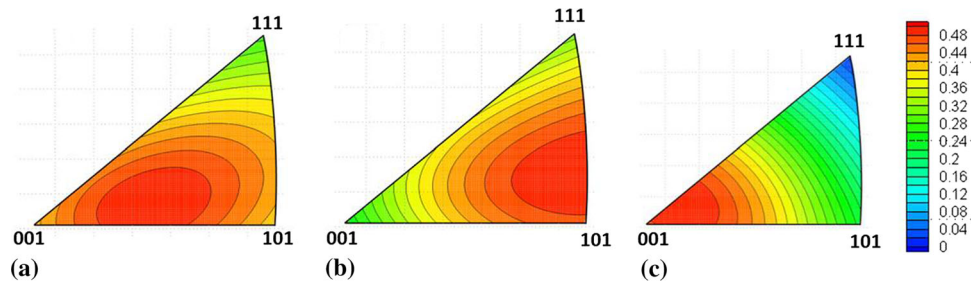


Fig. 12 Schmid factor contours for (a) slip, (b) twin under tensile stress, and (c) twin under compressive stress (Ref 27)

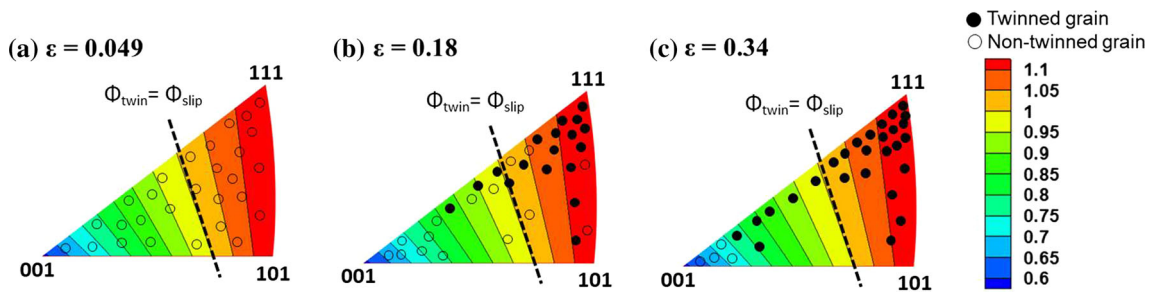


Fig. 13 Schmid factor analysis under tensile stress at the true strain of (a) 0.049, (b) 0.18, and (c) 0.34

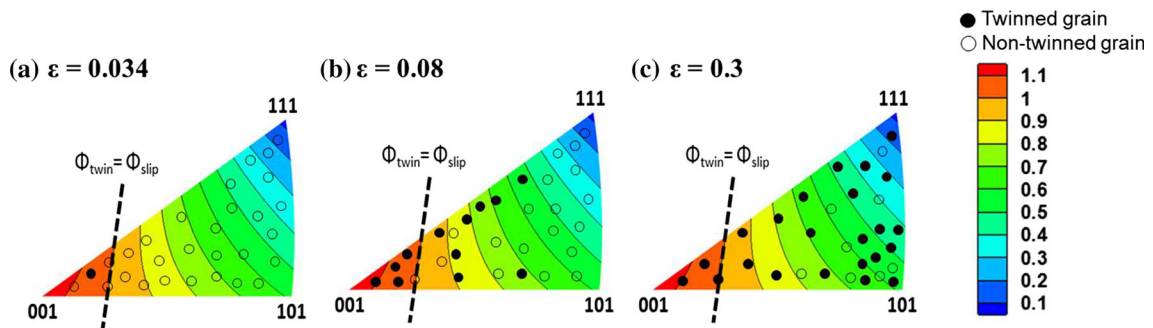


Fig. 14 Schmid factor analysis under compressive stress at the strain of (a) 0.034, (b) 0.08, and (c) 0.3

on EBSD maps shown in Fig. 3 and 4. It is worth emphasizing that twins tend to occur near $\langle 111 \rangle$ grains for tension and near $\langle 100 \rangle$ grains for compression; these orientations are twin-favorable regions in the Schmid factor contours. From these results, it is reasonable to note that the Schmid factor analysis well predicted the twinning behavior of TWIP steel in uniaxial tensile and compressive stress states. Although the twin-dominant region under compressive stress state is narrow compared to the tensile stress state, both Schmid factor for twin and slip under compressive stress are higher in this region than those under tensile stress. This can be one of the reasons to generate twins near $\langle 100 \rangle$ grains at lower strain under compressive stress since small amount of dislocation glides are necessary to make twins at low strain level (Ref 10, 13). In case of tension, the grains are rotated toward $\langle 111 \rangle$ and $\langle 100 \rangle$ by slip during deformation, and $\langle 111 \rangle$ is the twin-favorable orientation. Therefore, grain rotations activated the twin deformation mechanism (Ref 25). On the other hand, the grains are rotated toward $\langle 110 \rangle$ that is slip dominant orientation under compressive stress. Grain rotations by compression thus suppressed the twin deformation mechanism (Ref 26). This difference in grain rotations between the two stress states can make the different twinning behavior and microstructure during plastic deformation. The larger scattering of twinned grain within the Schmid factor contour under compressive stress was mainly originated from the orientation difference between twin generation $\langle 100 \rangle$ orientation and rotated stable $\langle 110 \rangle$ orientation.

Figure 15 shows the Schmid factor analysis during wire drawing based on the EBSD maps in Fig. 5. Grain rotation and twinning behavior were clearly seen in the Schmid factor contours. Strong $\langle 111 \rangle$ and weak $\langle 100 \rangle$ texture components were gradually developed at center area because center area was under the tensile stress state. At the strain of 0.13, twins occurred in less than 50% grains at center area, but most of the $\langle 111 \rangle$ grains had twins because $\langle 111 \rangle$ grains have the higher Schmid factor for twin under the tensile stress state. No twin appeared near $\langle 100 \rangle$ grain due to the lower Schmid factor of twin than that of slip under the tensile stress. On the other hand, all the grains of surface area had twins at the strain of 0.13 since both tensile and compressive stresses were

applied at the surface area. Furthermore, surface area had a higher strain compared to center area (Ref 35, 36). Apparently, the twins in grains close to $\langle 100 \rangle$ were originated by compressive stress and the twins in grains close to $\langle 111 \rangle$ and $\langle 110 \rangle$ were generated by tensile stress at surface area as explained in Fig. 13 and 14. These results explain why the surface area has more twin volume fraction (Fig. 7a), more twin variants (Fig. 7b), and more variety of twin thickness than the center area (Fig. 5). More interestingly, the texture and twinning behavior of center area were almost same as the specimen of tensile test: Strong $\langle 111 \rangle$ and weak $\langle 100 \rangle$ texture are developed, and twins appear in grains near $\langle 111 \rangle$ orientation not $\langle 100 \rangle$ orientation. This is due to the fact that only tensile stress was applied at center area of drawn wires (Ref 27). At the strain of 0.26, surface area also developed into tensile texture.

Figure 16 shows the Schmid factor analysis of caliber-rolled wire at the strain of 0.13 and 0.25 with area. The complex stress state during caliber rolling process made many twins at the early strain of 0.13. The $\langle 111 \rangle$ texture was developed at surface area because the overall stress state was tension at surface area (Ref 32). The main stress state of center area could be compression since the twinning behavior of center area was similar to the compressed specimen

3.4 Twinning Behaviors with Stress State

The most interesting feature of the present study is the different twin thickness, twin shape, twin variants, and twin volume fraction with stress state. The observed twinning behaviors with stress state are summarized in Table 2 and Fig. 17. Compared to the compressed specimens, tensile-strained specimens had a little bit thicker straight-type twins with more twin variant at the same strain. Center area of drawn wire had a similar twin structure to the tensile-strained specimen due to the tensile stress during wire drawing process, while surface area had a mixed twin structure with combined tensile and compressive stress states since tensile and compressive stresses were simultaneously applied at surface area. In case of caliber rolling, the complex stress state during process makes a similar twin structure to the surface area of drawn wire.

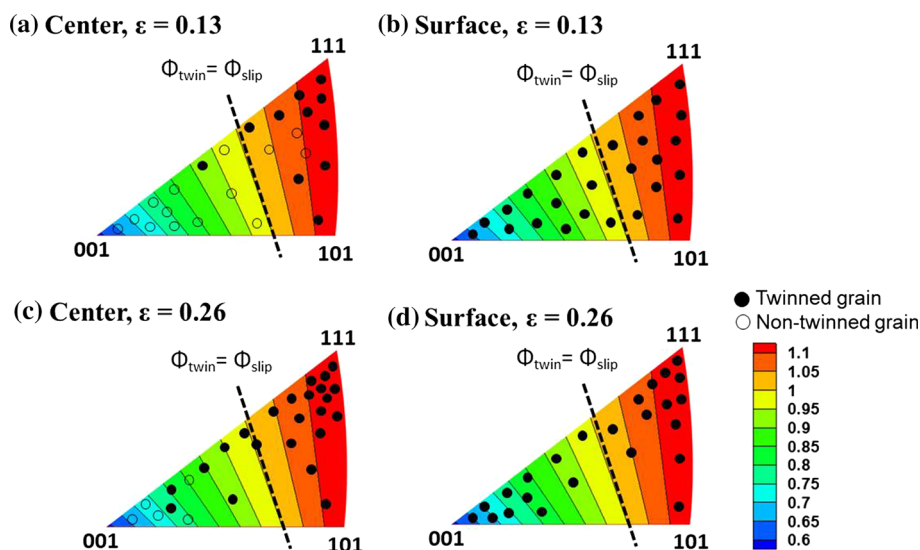


Fig. 15 Schmid factor analysis of drawn wire at the drawing strain of (a-b) 0.13 and (c-d) 0.26 with area

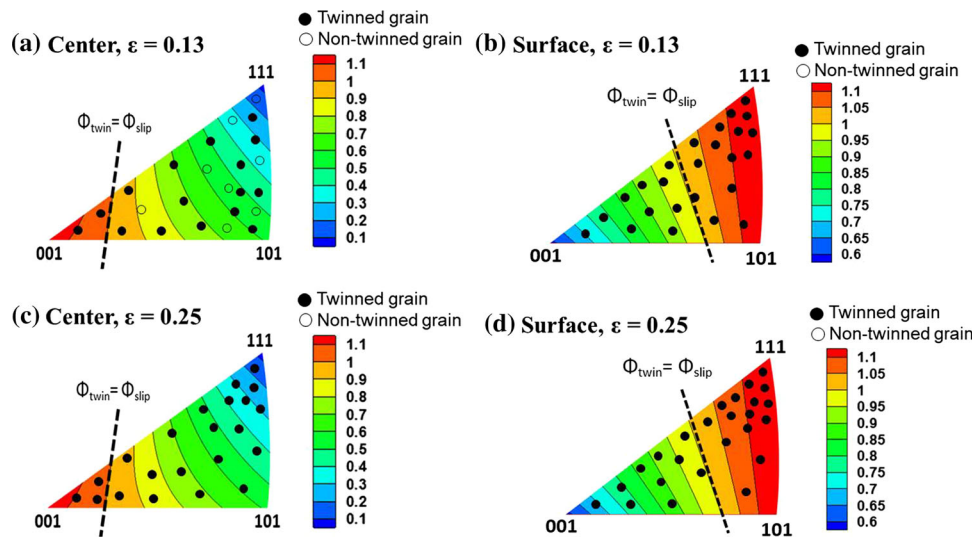


Fig. 16 Schmid factor analysis of caliber-rolled wire at the strain of (a-b) 0.13 and (c-d) 0.25 with area

Table 2 Comparison of twin structures and kinetics with stress state in TWIP steel

Stress state	Twin structures and kinetics						
	Thickness (average, nm)	Volume fraction	Shape	Twin variants	Twin bundles	Stable main texture	Main stress state
Tension	27	Low	Straight	2	Thick	Strong $\langle 111 \rangle$	Tension
Compression	22	Low	Wavy	1	Thin	Strong $\langle 110 \rangle$	Compression
<i>Wire drawing</i>							
Center	28	Low	Straight	2	Thick	Strong $\langle 111 \rangle$	Tension
Surface	21-29	High	Straight and wavy	2-3	Thick and thin	Less strong $\langle 111 \rangle$	Tension and compression
<i>Caliber rolling</i>							
Center	20-27	Very high	Wavy	2	Thin and thick	Less strong $\langle 110 \rangle, \langle 111 \rangle$	Compression and tension
Surface	23-30	High	Straight and wavy	2-3	Thick and thin	Strong $\langle 111 \rangle$	Tension and compression

It should be noted that the center area of caliber-rolled wire had a similar twin structure of compressed specimen because the compressive stress was dominant although tensile stress was also induced (Ref 32). These results confirmed that the tensile stress can make different twin structures in comparison with the compressive stress, which means stress state strongly affected the twinning behaviors.

According to the Schmid factor analysis, tensile stress encouraged the occurrence of deformation twinning since the grains rotate to the $\langle 111 \rangle$ orientation, which is twinning-favorable orientation. On the other hand, compressive stress suppressed the occurrence of twinning because the grains rotate to the $\langle 110 \rangle$ orientation, which is slip-favorable orientation. It is well known that deformation twin in metals is generated by pre-existing dislocation configurations that separate into multilayered stacking fault structures. Although several researchers have proposed different dislocation-based twinning mechanisms (Ref 56-59), most of the mechanisms involve the glide of Shockley partial dislocations on the successive (111) planes to create twins. Passage of Shockley partial dislocation on the first layer generated a stacking fault,

and the next second and third partial dislocations on successive (111) planes generated a three-layer twin stacking fault. Therefore, passage of more partials on successive (111) planes led to formation of thick twins (Ref 58). That is, twin was nucleated and then grown with strain during the plastic deformation. Typically, the stress required to nucleate twins has been determined by the twin sources such as dislocation pile up and Lomer-Cottrell lock. Meanwhile, twin growth was related to the SFE, strain rate, stress state, etc. Under tensile stress, the grain rotation to $\langle 111 \rangle$ orientation, twinning-favored region, encouraged the lateral growth of twins by the gradual emission of new partial dislocations, resulting in relatively thick twins, while the grain rotation to $\langle 110 \rangle$ orientation under compressive stress suppressed the twin growth since twin was difficult to occur in this orientation due to lower Schmid factor for twin rather than slip. This is the main reason why tensile-strained specimen had thicker twins in comparison with compressive-strained specimen. The difference in twin bundle thickness between tensile and compressive-strained specimens was also explained by the same mechanism above.

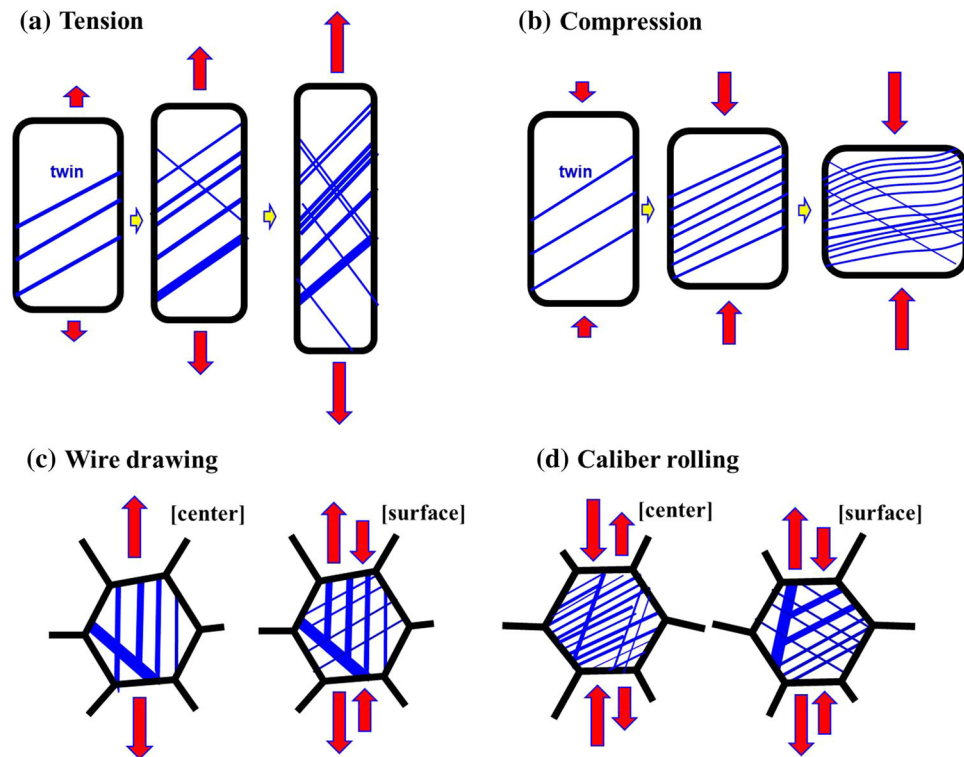


Fig. 17 Schematic showing the influence of stress state on twinning behaviors in TWIP steel

The wavy-shaped twins in compressive-strained specimen were also highly related to the grain rotation during plastic deformation. The grains close to $\langle 100 \rangle$ orientation having deformation twins rotated to $\langle 101 \rangle$ orientation by slip; grain rotation by slip makes the straight-type twin initially generated close to $\langle 100 \rangle$ orientation wavy shape or distorted. At higher strain, it is difficult to observe these wavy-type twins by EBSD. On the other hand, the tensile-strained specimen had straight-shaped twins because the twins made in grains near $\langle 111 \rangle$, where Schmid factor is higher for twins than slip, do not rotate, resulting in straight-type twins, and finally are well observed by EBSD. That is, this interaction of twin and slip with the help of grain rotation during plastic deformation can make the wavy- or straight-shaped twins.

The difference in the number of twin variants with stress state was also related to the grain rotation. Compressive stress suppressed the twinning activity as shown in Schmid factor analysis. The grains near $\langle 100 \rangle$ orientation with deformation twins were rotated easily and quickly to $\langle 110 \rangle$ orientations, where slip favored region, which prevent developing the other twinning system at the same grain. In contrast, under tensile stress, the grains near $\langle 111 \rangle$ orientation with T1 sustained the same orientation, where twin favored region, which activated the other twinning systems. In addition, the grains tend to rotate from twin-unfavorable region to twin-favorable region by slip, which gradually increased the twin variants with strain during tensile test.

Higher twin volume fraction in compressive-strained specimen compared to the tensile-strained specimen was much less understood in this study. This can be related to the evaluation of twin volume fraction by total twin length. That is, both twin length and twin width need to be considered to measure the twin volume fraction; however, only twin length was consid-

ered to measure the total twin length. In addition, it is observed that only larger twins can be recognized by EBSD analysis software. That is, the fine twins are not selected in the EBSD software due to the lower Kikuchi band contrast and step size even though they are observed in image quality map. Measuring the twin length as well as the limitation of measuring the twin length by EBSD technique may be attributed to the contradiction on twin volume fraction between compressed specimens and tensile-strained specimens. However, additional systematic investigation is necessary to fully understand the underlying twin mechanism with stress state, especially twin volume fraction.

Drawn and caliber-rolled wires had both twin structures under tensile and compressive stresses and higher twin volume fraction since complex stress states that combined tension and compression were applied in these processes. Inversely, we can find out the applied stress state of specimen by observing the twin structures and kinetics.

4. Conclusions

Based on the comparison study on twinning behaviors with different stress states such as tension, compression, wire drawing, and caliber rolling in TWIP steel, the following major conclusions can be drawn:

1. Twin structures such as twin thickness, twin variants, and twin shape, and twin kinetics were different with stress states. The specimen under compressive stress had wavy-shaped twins, less twin variants, low twin thickness, and more twin volume fraction in comparison with the specimen under tensile stress.

2. The different structures and kinetics of deformation twin with stress state were highly related to the grain rotation during plastic deformation. Under tensile stress, the grain rotation to $\langle 111 \rangle$ orientation, twinning-favorable region by Schmid factor analysis, encouraged the lateral growth of twins, more twin variants, and straight-type twins. On the other hand, the grain rotation to $\langle 110 \rangle$ orientation under compressive stress suppressed the twin growth and more twin variants and developed wavy-shaped twin since twin was difficult to occur in this orientation due to lower Schmid factor for twin rather than slip.
3. Drawn wire and caliber-rolled wire had both twin features under tension and compression and higher twin kinetics since complex stress state that combined tension and compression was applied in these processes.
4. The hardness values with strain state were strongly related to the twin volume fraction: Both twin volume fraction and average hardness were larger for caliber rolling, wire drawing then compression, and finally tension.

Acknowledgments

This Research was supported by the Tongmyong University Research Grants 2018 (2018A016-1).

References

1. O. Bouaziz, S. Allain, C.P. Scott, P. Cugy, and D. Barbier, High Manganese Austenitic Twinning Induced Plasticity Steels: A Review of the Microstructure Properties Relationships, *Curr. Opin. Solid State Mater. Sci.*, 2011, **15**, p 141–168
2. O. Grassel, L. Kruger, G. Frommeyer, and L.W. Meyer, High Strength Fe-Mn-(Al, Si) TRIP/TWIP Steels Development-Properties-Application, *Int. J. Plast.*, 2000, **16**, p 1391–1409
3. B.C. De Cooman, Y. Estrin, and S.K. Kim, Twinning-Induced Plasticity (TWIP) Steels, *Acta Mater.*, 2018, **142**, p 283–362
4. I. Gutierrez-Urrutia, S. Zaefferer, and D. Raabe, The Effect of Grain Size and Grain Orientation on Deformation Twinning in a Fe-22Mn-0.6C TWIP Steel, *Mater. Sci. Eng. A*, 2010, **527**, p 3552–3560
5. R. Ueji, Y. Takagi, N. Tsuchida, K. Shinagawa, Y. Tanaka, and T. Mizuguchi, Crystallographic Orientation Dependence of e-Martensite Transformation During Tensile Deformation of Polycrystalline 30% Mn Austenitic Steel, *Mater. Sci. Eng. A*, 2013, **576**, p 14–20
6. Y.N. Dastur and W.C. Leslie, Mechanism of Work Hardening in Hadfield Manganese Steel, *Metall. Trans. A*, 1981, **12**, p 749–759
7. L. Chen, H.S. Kim, S.K. Kim, and B.C. DeCooman, Localized Deformation Due to Portevin–LeChatelier Effect in 18Mn-0.6C TWIP Austenitic Steel, *ISIJ Int.*, 2007, **47**, p 1804–1812
8. L. Qian, P. Guo, F. Zhang, J. Meng, and M. Zhang, Abnormal Room Temperature Serrated Flow and Strain Rate Dependence of Critical Strain of a Fe-Mn-C Twin-Induced Plasticity Steel, *Mater. Sci. Eng. A*, 2013, **561**, p 266–269
9. S.J. Lee, J. Kim, S.N. Kane, and B.C. De Cooman, On the Origin of Dynamic Strain Aging in Twinning-Induced Plasticity Steels, *Acta Mater.*, 2011, **59**, p 6809–6819
10. I. Karaman, H. Sehitoglu, A. Beaudoin, Y.I. Chumlyakov, H.J. Maier, and C.N. Tome, Modeling the Deformation Behavior of Hadfield Steel Single and Polycrystals Due to Twinning and Slip, *Acta Mater.*, 2000, **48**, p 2031–2047
11. O. Bouaziz, S. Allain, and C. Scott, Effect of Grain and Twin Boundaries on the Hardening Mechanisms of Twinning-Induced Plasticity Steels, *Scr. Mater.*, 2008, **58**, p 484–487
12. J.G. Sevillano, An Alternative Model for the Strain Hardening of FCC Alloys That Twin, Validated for Twinning-Induced Plasticity Steel, *Scr. Mater.*, 2009, **60**, p 336–339
13. D. Barbier, N. Gey, S. Allain, N. Bozzolo, and M. Humbert, Analysis of the Tensile Behavior of a TWIP Steel Based on the Texture and Microstructure Evolutions, *Mater. Sci. Eng. A*, 2009, **500**, p 196–206
14. K. Renard and P.J. Jacques, On the Relationship Between Work Hardening and Twinning Rate in TWIP Steels, *Mater. Sci. Eng. A*, 2012, **542**, p 8–14
15. J.E. Jin and Y.K. Lee, Strain Hardening Behavior of a Fe-18Mn-0.6C-1.5Al TWIP Steel, *Mater. Sci. Eng. A*, 2009, **527**, p 157–161
16. J.E. Jin and Y.K. Lee, Effect of Al on Microstructure and Tensile Properties of C-Bearing High Mn TWIP Steel, *Acta Mater.*, 2012, **60**, p 1680–1688
17. I. Gutierrez-Urrutia and D. Raabe, Dislocation and Twin Substructure Evolution During Strain Hardening of an Fe-22Mn-0.6C TWIP Steel Observed by Electron Channeling Contrast Imaging, *Acta Mater.*, 2011, **59**, p 6449–6462
18. S. Allain, J.P. Chateau, O. Bouaziz, S. Migot, and N. Guelton, Correlations Between the Calculated Stacking Fault Energy and the Plasticity Mechanisms in Fe-Mn-C Alloys, *Mater. Sci. Eng. A*, 2004, **387–389**, p 158–162
19. A. Saeed-Akbari, J. Imlau, U. Prahl, and W. Bleck, Derivation and Variation in Composition-Dependent Stacking Fault Energy Maps Based on Subregular Solution Model in High-Manganese Steels, *Metall. Mater. Trans. A*, 2009, **40**, p 3076–3090
20. S. Curtze and V.T. Kuokkala, Dependence of Tensile Deformation Behavior of TWIP Steels on Stacking Fault Energy, Temperature and Strain Rate, *Acta Mater.*, 2010, **58**, p 5129–5141
21. J.K. Kim and B.C. De Cooman, Stacking Fault Energy and Deformation Mechanisms in Fe-xMn-0.6C-yAl TWIP Steel, *Mater. Sci. Eng. A*, 2016, **676**, p 216–231
22. I. Karaman, H. Sehitoglu, K. Gall, Y.I. Chumlyakov, and H.J. Maier, Deformation of Single Crystal Hadfield Steel by Twinning and Slip, *Acta Mater.*, 2000, **48**, p 1345–1359
23. L. Brake, L. Kestens, and J. Penning, Direct Observation of the Twinning Mechanism in an Austenitic Fe-Mn-C Steel, *Scr. Mater.*, 2009, **61**, p 220–222
24. S. Sato, E.P. Kwon, M. Imafuku, K. Wagatsuma, and S. Suzuki, Microstructural Characterization of High-Manganese Austenitic Steels with Different Stacking Fault Energies, *Mater. Charact.*, 2011, **62**, p 781–788
25. P. Yang, Q. Xie, L. Meng, H. Ding, and Z. Tang, Dependence of Deformation Twinning on Grain Orientation in a High Manganese Steel, *Scr. Mater.*, 2006, **55**, p 629–631
26. L. Meng, P. Yang, Q. Xie, H. Ding, and Z. Tang, Dependence of Deformation Twinning on Grain Orientation in Compressed High Manganese Steels, *Scr. Mater.*, 2007, **56**, p 931–934
27. J.K. Hwang, I.C. Yi, I.H. Son, J.Y. Yoo, B. Kim, A. Zargarani, and N.J. Kim, Microstructural Evolution and Deformation Behavior of Twinning-Induced Plasticity (TWIP) Steel During Wire Drawing, *Mater. Sci. Eng. A*, 2015, **644**, p 41–52
28. K. Renard, H. Idrissi, D. Schryvers, and P.J. Jacques, On the Stress State Dependence of the Twinning Rate and Work Hardening in Twinning-Induced Plasticity Steels, *Scr. Mater.*, 2012, **66**, p 966–971
29. H. Idrissi, K. Renard, D. Schryvers, and P.J. Jacques, On the Relationship Between the Twin Internal Structure and the Work Hardening Rate of TWIP Steels, *Scr. Mater.*, 2010, **63**, p 961–964
30. M. Ghasri-Khouzani and J.R. McDermid, Effect of Carbon Content on the Mechanical Properties and Microstructure Evolution of Fe-22Mn-C Steels, *Mater. Sci. Eng. A*, 2015, **621**, p 118–127
31. J.K. Hwang, I.H. Son, J.Y. Yoo, A. Zargarani, and N.J. Kim, Effect of Reduction of Area on Microstructure and Mechanical Properties of Twinning-Induced Plasticity Steel During Wire Drawing, *Met. Mater. Int.*, 2015, **21**, p 815–822
32. J.K. Hwang, Effects of Caliber Rolling on Microstructure and Mechanical Properties in Twinning-Induced Plasticity (TWIP) Steel, *Mater. Sci. Eng. A*, 2018, **711**, p 156–164
33. K. Jeong, J.E. Jin, Y.S. Jung, S. Kang, and Y.K. Lee, The Effects of Si on the Mechanical Twinning and Strain Hardening of Fe-18Mn-0.6C Twinning-Induced Plasticity Steel, *Acta Mater.*, 2013, **61**, p 3399–3410
34. M.G. Stout and J.A. O'Rourke, Experimental Deformation Textures of OFE Copper and 70:30 Brass From Wire Drawing, Compression, and Torsion, *Metall. Trans. A*, 1989, **20A**, p 125–131
35. R.K. Chin and P.S. Stelf, A Computational Study of Strain Inhomogeneity in Wire Drawing, *Int. J. Mach. Tools Manuf.*, 1995, **35**, p 1087–1098

36. G.H. Hasani, R. Mahmudi, and A. Karimi-Taheri, On the Strain Inhomogeneity in Drawn Copper Wires, *Int. J. Mater. Form.*, 2010, **3**, p 59–64
37. J.K. Hwang, Drawing Direction Effect on Microstructure and Mechanical Properties of Twinning-Induced Plasticity Steel During Wire Drawing, *J. Mater. Eng. Perform.*, 2019, **28**, p 2834–2844
38. J. Chen, W. Yan, C.X. Liu, R.G. Ding, and X.H. Fan, Dependence of Texture Evolution on Initial Orientation in Drawn Single Crystal Copper, *Mater. Charact.*, 2011, **62**, p 237–242
39. A.A. Saleh, E.V. Pereloma, and A.A. Gazder, Texture Evolution of Cold Rolled and Annealed Fe-24Mn-3Al-2Si-1Ni-0.06C TWIP Steel, *Mater. Sci. Eng. A*, 2011, **528**, p 4537–4549
40. G. Palumbo and K.T. Aust, Structure-Dependence of Intergranular Corrosion in High Purity Nickel, *Acta Metall. Mater.*, 1990, **38**, p 2343–2352
41. C. Efstathiou and H. Sehitoglu, Strain Hardening and Heterogeneous Deformation During Twinning in Hadfield Steel, *Acta Mater.*, 2010, **58**, p 1479–1488
42. Y.S. Jung, S. Kang, K. Jeong, J.G. Jung, and Y.K. Lee, The Effects of N on the Microstructures and Tensile Properties of Fe-15Mn-0.6C-2Cr-xN Twinning-Induced Plasticity Steels, *Acta Mater.*, 2013, **61**, p 6541–6548
43. H.K. Yang, Z.J. Zhang, and Z.F. Zhang, Comparison of Work Hardening and Deformation Twinning Evolution in Fe-22Mn-0.6C-(1.5Al) Twinning-Induced Plasticity Steels, *Scr. Mater.*, 2013, **68**, p 992–995
44. S. Mahajan and G.Y. Chin, Twin–Slip, Twin–Twin and Slip–Twin Interactions in Co-8 wt.% Fe Alloy Single Crystals, *Acta Metall.*, 1973, **21**, p 173–179
45. P. Mullner, C. Solenthaler, and M.O. Speidel, Second Order Twinning in Austenitic Steel, *Acta Metall. Mater.*, 1994, **42**, p 1727–1732
46. M. Bonisch, Y. Wu, and H. Sehitoglu, Hardening by Slip–Twin and Twin–Twin Interactions in FeMnNiCoCr, *Acta Mater.*, 2018, **153**, p 391–403
47. A. Stukowski and K. Albe, Nanotwinned fcc Metals: Strengthening Versus Softening Mechanisms, *Phys. Rev. B*, 2010, **82**, p 224103
48. S. Alkan, A. Ojha, and H. Sehitoglu, Determination of Latent Hardening Response for FeNiCoCrMn for Twin–Twin Interactions, *Acta Mater.*, 2018, **147**, p 149–164
49. H.K. Yang, Y.Z. Tian, Z.J. Zhang, and Z.F. Zhang, Simultaneously Improving the Strength and Ductility of Fe-22Mn-0.6C Twinning-Induced Plasticity Steel Via Nitrogen Addition, *Mater. Sci. Eng. A*, 2018, **715**, p 276–280
50. T.S. Byun, On the Stress Dependence of Partial Dislocation Separation and Deformation Microstructure in Austenitic Stainless Steels, *Acta Mater.*, 2003, **51**, p 3063–3071
51. S.M. Lee, S.J. Lee, S. Lee, J.H. Nam, and Y.K. Lee, Tensile Properties and Deformation Mode of Si-Added Fe-18Mn-0.6C Steels, *Acta Mater.*, 2018, **144**, p 738–747
52. K.T. Park, K.G. Jin, S.H. Han, S.W. Hwang, K. Choi, and C.S. Lee, Stacking Fault Energy and Plastic Deformation of Fully Austenitic High Manganese Steels: Effect of Al Addition, *Mater. Sci. Eng. A*, 2010, **527**, p 3651–3661
53. V. Shterner, L.B. Timokhina, A.D. Rollett, and H. Beladi, The Role of Grain Orientation and Grain Boundary Characteristics in the Mechanical Twinning Formation in a High Manganese Twinning-Induced Plasticity Steel, *Metall. Mater. Trans. A*, 2018, **49**, p 2597–2611
54. H. Beladi, I.B. Timokhina, Y. Estrin, J. Kim, B.C. De Cooman, and S.K. Kim, Orientation Dependence of Twinning and Strain Hardening Behaviour of a High Manganese Twinning Induced Plasticity Steel with Polycrystalline Structure, *Acta Mater.*, 2011, **59**, p 7787–7799
55. S. Kibey, J.B. Liu, D.D. Johnson, and H. Sehitoglu, Energy Pathways and Directionality in Deformation Twinning, *Appl. Phys. Lett.*, 2007, **91**, p 181916
56. A.H. Cottrell and B.A. Bilby, A Mechanism for the Growth of Deformation Twins in Crystals, *Philos. Mag.*, 1951, **42**, p 573–581
57. J.A. Venables, Deformation Twinning in Face-Centred Cubic Metals, *Philos. Mag.*, 1961, **6**, p 379–396
58. S. Mahajan and G.Y. Chin, Formation of Deformation Twins in fcc Crystals, *Acta Metall.*, 1973, **21**, p 1353–1363
59. T. Mori and H. Fujita, Dislocation Reactions During Deformation Twinning in Cu-11 at.% Al Single Crystals, *Acta Metall.*, 1980, **28**, p 771–776

Publisher's Note Springer Nature remains neutral with regard to jurisdictional claims in published maps and institutional affiliations.